Manufacturing and performances of MnZn ferrite cores with thin walls prepared by paste material extrusion 3D printing

Aziz Zekhnini, Gérard Delette, Anne-Lise Adenot-Engelvin, Olivier Isnard

Additive Manufacturing 92 (2024) 104389

Contents lists available at ScienceDirect

Additive Manufacturing

journal homepage: www.elsevier.com/locate/addma

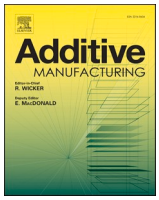

Manufacturing and performances of MnZn ferrite cores with thin walls prepared by paste material extrusion 3D printing

A. Zekhnini [a,c,*], G. Delette [a], A.L. Adenot-Engelvin [b], O. Isnard [c]

[a] Univ. Grenoble Alpes, CEA, LITEN, DTNM, 17 Avenue des Martyrs, Grenoble 38054, France
[b] CEA-DAM, Le Ripault, BP16, Monts 37260, France
[c] Univ. Grenoble Alpes, Institut Néel du CNRS, BP166, 25 Avenue des Martyrs, Grenoble 38042, France

ARTICLE INFO

Keywords:
Additive Manufacturing
3D printing
Material extrusion
MnZn ferrite
Magnetic permeability
Core loss

ABSTRACT

The 3D printing technique using material extrusion of a paste filled with ferrite powder $(Mn,Zn)Fe_2O_4$ and organic additives has been successfully improved to produce sintered samples for studying their magnetic and structural properties. The rheological behaviour of the pastes and the printing parameters have been optimised to obtain parts with regular geometries, in particular by minimising sagging effect during filament deposition. Printing is followed by a debinding and sintering stage, for which the temperature and oxygen partial pressure conditions were adjusted. These conditions enable the densification of the $(Mn,Zn)Fe_2O_4$ material in the spinel structure without parasitic phases, with a low grain size dispersion and a relative density of 91 %. The core loss has been measured on the 3D printed samples to be 144 mW/cm^3 at a frequency of 500 kHz and an induction of 50 mT. This performance is comparable to the nominal value of a part produced by the conventional process. This work paves the way for an advantageous manufacturing method in terms of accessible geometries, while maintaining satisfactory magnetic characteristics.

1. Introduction

Spinel structure ferrites $(Mn,Zn)Fe_2O_4$ are widely used as soft magnetic materials for passive components (transformers, inductors) operating up to several MHz in power electronics applications, such as power converters [1,2]. Conventionally, magnetic cores are shaped on an industrial scale to a wide variety of geometries using powder metallurgy processes. However, the current trend towards higher switching frequencies in power converters requires innovative core designs in order to limit the power losses and induced heating of the component. More particularly, improving the thermal management of small-sized magnetic cores is becoming a challenge for designers. Unconventional geometries have recently been considered to enhance the thermal regulation of $(Mn,Zn)Fe_2O_4$-based transformers, integrating for example drains or fins into the core [3,4]. However, traditional manufacturing methods based on die pressing and sintering fail to produce such complex geometries without involving costly machining operations.

The use of MnZn ferrite material at high frequency requires minimizing the dynamic losses in magnetic cores. Andalib et al. have shown that the contribution to the losses of the eddy current becomes significant above 500 kHz [5]. In order to reduce these losses, several solutions have been investigated: reducing the grain size [6], increasing the effective resistivity [5] and increasing the shape ratio (height/width) of the cores [7]. In this work, we focus on the use of additive manufacturing (AM) to mitigate the dependence of the eddy current loss on the dimensions of MnZn cores.

Several studies have also shown the interest of designing ferrite-based components with small geometrical details to improve the high frequency operation [8,9]. These promising results are leading to envisage the manufacture of magnetic cores using AM techniques [10–14]. To date, very few studies have described the AM of dense Mn-Zn ferrite-based components [11]. This last work has shown the possibility of obtaining parts using indirect AM methods such as stereolithography (SLA). However, the low density achieved on these parts leads to poor performances, which is an obstacle when looking for applications in power electronics. This limitation is inherent to the commercial photopolymerisation machines currently available, whose photon beam energy located in the ferrite absorption band. Consequently, these machines are only effective for low contents of ferrite powder. In SLA, the ferrite particles strongly absorb the UV radiation preventing the paste to be efficiently cured by photopolymerisation [11].

* Corresponding author at: Univ. Grenoble Alpes, CEA, LITEN, DTNM, 17 Avenue des Martyrs, Grenoble 38054, France.
E-mail addresses: aziz.zekhnini@cea.fr, zekhniniaziz95@gmail.com (A. Zekhnini), gerard.delette@cea.fr (G. Delette).

https://doi.org/10.1016/j.addma.2024.104389
Received 9 February 2024; Received in revised form 12 July 2024; Accepted 26 August 2024
Available online 30 August 2024

3D printing techniques, in particular the material extrusion of powder-loaded pastes, also known as robocasting or DIW (Direct Ink Writing) [15–18] offers a solution by making it possible to increase the powder loading rate while ensuring sufficient resolution for the manufacture of components with dimensions of a few tenths of a millimetre. This extrusion process requires precise control of the printing parameters and the rheological properties of the pastes to obtain regularly shaped parts that resist deformation and sagging of the filaments deposited during extrusion [13,19–21]. Accordingly, the process parameters should be carefully adapted to the given powder in order to print parts that remain geometrically stable after extrusion.

This article describes in detail the various stages in the manufacture of dense MnZn ferrite-based parts formed by the material extrusion process (Fig. 1). The interest lies firstly in the development of an organic paste filled with $(Mn,Zn)Fe_2O_4$ powder that is compatible with 3D robocasting. Secondly, the conditions for using this paste to produce dense toroidal parts will be presented. Two types of heat treatment were studied to densify the printed samples. The part is first debinded using a heat treatment designed to gradually degrade the organic constituents while maintaining the part's geometry. The green part is then densified by high-temperature sintering in an oxidising atmosphere. These conditions enable the spinel crystalline phase to be formed, while controlling the degree of oxidation of the various cations and achieving the desired magnetic properties.

Finally, the last section is devoted to the characterisation of microstructures and the measurements of dynamic magnetic permeability, followed by the characterisation of core losses. Samples formed by the standard process of uniaxial compression in die and sintering, from the same powder, were used as a reference in this study to help interpret and discuss the results. These reference samples will be noted T-Std and those obtained by robocasting will be named T-AM.

2. Materials and methods

2.1. Preparation of the feedstocks

The printable pastes are generally composed of powders mixed with organic additives such as solvents, binders, plasticisers and dispersants. In this study, two paste formulations composed of 82 wt% (48 vol%) ceramic powder were prepared in order to analyse their rheological behaviour and their suitability for extrusion through metal nozzles. These two hydrogel-based formulations F#1 and F#2 were studied for dispersing Mn-Zn ferrite ceramic powder. The hydrogel in formulation F#1 is formed by solubilising a 20 wt% PEO-PPO-PEO triblock copolymer (Pluronic F-127, Sigma Aldrich, France) in distilled water at 4 °C. The temperature was chosen to avoid gelation of the hydrogel, which occurs at around 18 °C [22]. Dissolution was achieved by three successive additions of Pluronic F-127, between which the solution was kept at 4 °C. The solution was then homogenised in a planetary centrifugal mixer (Kurabo Mazerustar KK-400 WE, Japan). The hydrogel in formulation F#2 is made from Pluronic F-127 and a binder, PVA (Polyvinyl alcohol, Acros Organics, USA) in equal mass fractions. First, the PVA was dissolved in water at 80 °C under magnetic stirring for 2 hours. Once a homogeneous solution was obtained, the solution was cooled to 4 °C and mixed with the solution containing the Pluronic F-127 binder, as shown in Fig. 1a. The dispersant (Diperbyk 111, BYK, Germany) was then added to the two hydrogels before homogenisation in a planetary centrifugal mixer. The advantage of this second formulation is that it modifies the hydrogel's gelling temperature [23] and viscosity, making it easier to print.

The dispersion step of manganese zinc ferrite powder $(Mn,Zn)Fe_2O_4$ (Z70-L2G, JMC, Japan) is illustrated in Fig. 1b. This ready-to-press commercial powder is atomised and bonded with PVA, as shown by scanning electron microscopy (SEM LEO-1530, ZEISS, Germany) in Fig. 2. The powder grains consist of an agglomeration of primary particles smaller than 1 μm to form toroidal secondary larger particles (10–130 μm). The powder was heat treated at 400 °C for 3 hours to remove the PVA and facilitate its dispersion in the hydrogel.

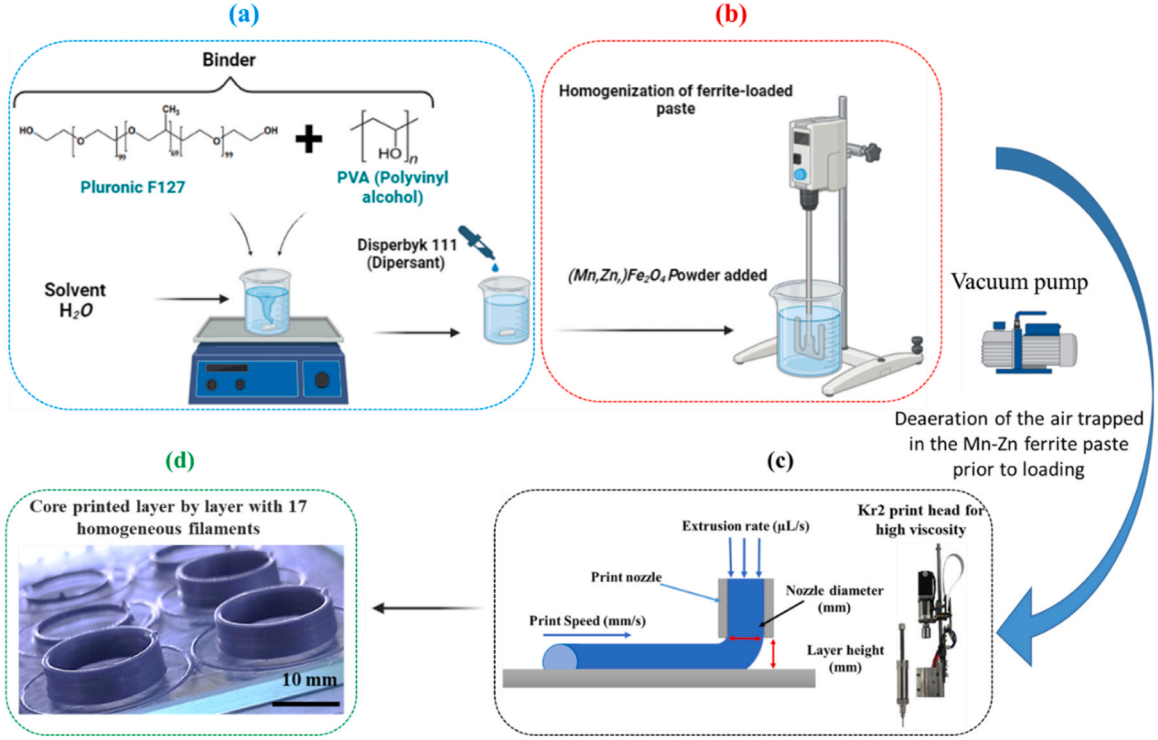

Fig. 1. Diagram illustrating the steps involved in preparing paste 2 (F#2) and the principle of printing MnZn ferrite cores.

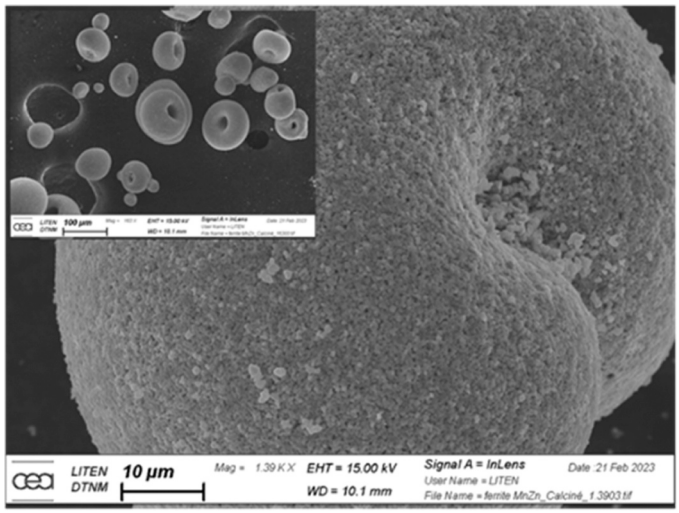

Fig. 2. Morphology of $(Mn,Zn)Fe_2O_4$ ferrite powder as observed by scanning electron microscopy (SEM).

The powder is dispersed (48 vol%) in the two hydrogels in three stages, with intervals for cooling the paste to 4 °C after the addition of each third. This stage is followed by homogenisation of the formulation using a planetary mixer. A mixing stage using a tricyclindrical mixer is necessary to be able to print homogeneous filaments owing to smaller and more uniform agglomerates well dispersed in the paste that prevents clogging of the printhead nozzle. The final step in preparing the feedstock involves degassing the paste to eliminate the air trapped during the mixing stages. This degassing was carried out in a crystalliser using a primary vacuum pump (P= 10^{-3} mbar) to evacuate the air.

Table 1 shows the mass quantities of each component in the two tested formulations F#1 and F#2. Thermogravimetric analysis (TGA) (STA 449 F1 Jupiter analyzer, Netzsch, Germany) was used to check the mass percentage of each component in the two formulations prepared, and enabled us to define the debinding cycle by determining the total degradation temperature of the organic additives. These measurements were carried out in air at a heating rate of 5 °C/min up to 600 °C, followed by a 1-hour stage at 600 °C.

Shaping by 3D printing using the material extrusion technique requires the rheological properties of the paste to be characterised. Measurements of viscosity as a function of shear rate that were carried out using a rheometer (Kinexus Pro+, Netzsch, Germany) with parallel plates. The measurements were carried out at a temperature of 25 °C, with a planar geometry of 20 mm diameter and a gap of 0.8 mm over a shear rate range from 0.1 s^{-1} to 100 s^{-1}.

2.2. Configuration of the 3D printing equipment

The part to be printed is defined beforehand using computer-aided design (CAD) software. The CAD file is sent to the printing machine's control system, which monitor the movements of the print head. A torus model has been defined to produce the samples required for magnetic characterizations. Fig. 1c shows the print head (Kr2–15) of the 3D printer (Hydra 16a, Hyrel 3D, USA), as well as the operating principle of this technique, which is based on the deposition of the extruded bead by direct contact with a non-stick substrate using a mobile metal nozzle. The use of a metal nozzle with a diameter of 1 mm enabled to print pastes with a high powder content, which guarantees a high green density and minimises part shrinkage during drying and heat treatment, either during debinding or sintering.

Printing parameters include layer height (Z_0, mm), printing speed (V, mm/s), and nozzle diameter (D, mm). These parameters have been carefully adjusted according to the experimental conditions, in particular temperature and humidity. The temperature of the printing substrate was adjusted in order to obtain geometries with minimal layer sagging during deposition.

Table 1
Composition of paste 1 and paste 2.

Components	Paste 1 (F#1)	Weight (g)	Paste 2 (F#2)	Weight (g)
Powder	$(Mn,Zn)Fe_2O_4$	72.16	$(Mn,Zn)Fe_2O_4$	72.16
Solvent	De-ionized Water	12.32	De-ionized Water	12.32
Binder	Pluronic F−127	3.08	Pluronic F−127	1.54
			PVA	1.54
Dispersant	Disperbyk 111	0.44	Disperbyk 111	0.44

2.3. Thermal debinding and sintering conditions

Printed parts require the removal of organic additives before proceeding to the sintering stage. The thermal debinding conditions are selected on the basis of preliminary thermogravimetric analysis (TGA) carried out in air on the unfilled polymer mixtures. The cores were therefore thermally debinded in a resistive ceramic oven in air, at temperature levels detailed in Section 3.3 for 6 h to eliminate all organic residues, with a slow ramp of 0.5 °C/min to avoid cracking in the printed parts during the temperature rise.

To compare and evaluate the properties of printed parts (AM), the uniaxial compression manufacturing technique was used to produce reference parts. A 20 mm diameter cylindrical mold was used to produce reference cores, and a 9 mm diameter mold was used to produce disks for dilatometry analysis. All reference parts were compacted at a pressure of 200 MPa. The feedstock prepared for 3D printing was used to manufacture these reference parts. This feedstock was compacted after natural drying. The cores formed by this standard process (T-Std.) and robocasting (T-AM) were subjected to the same sintering process in a tube furnace, maintained at an oxygen partial pressure of 0.7 %. In order to determine the sintering temperature, the longitudinal shrinkage was previously determined using a dilatometer (Setaram Setsys Evolution TMA, France). Density and open porosity were measured on sintered samples by the Archimedes method using ethanol and at an ambient temperature of 25 °C.

2.4. Samples characterization

Microscopic observations were made using a scanning electron microscope (SEM LEO-1530, ZEISS, Germany), and grain size analysis was carried out by image analysis using ImageJ software [24]. X-ray diffraction patterns were obtained using a diffractometer (Bruker D8 Endeavour, Germany) with a copper radiation source ($K_{\alpha1}$ = 1.54060 Å, $K_{\alpha2}$ = 1.54439 Å) to detect the phases formed as a function of each sintering temperature applied to the printed cores.

The cores produced by robocasting (T-AM) and standard process (T-Std.) after heat treatment are wounded and the inductance formed is characterized using an impedance analyzer (Keysight E4990A Impedance Analyzer, USA). The relative permeability values are deduced from impedance measurement according to the approach described in Appendix 1. B-H loops were measured on the standard sample with the hysteresisgraph (AMH-1 M-S, Labotorio Elettrofisico, Italy) at two frequencies (1 kHz, 10 kHz) and at applied fields (700 A/m). The method used to measure losses in magnetic cores is described in references [25, 26].

3. Experimental results

3.1. Rheological properties of feedstocks

The curve plotted in Fig. 3a shows that both formulations prepared (F#1 and F#2) exhibit rheofluidising or pseudoplastic behaviour. This behaviour is characterized by a decrease in viscosity η as the shear rate $\dot{\gamma}$

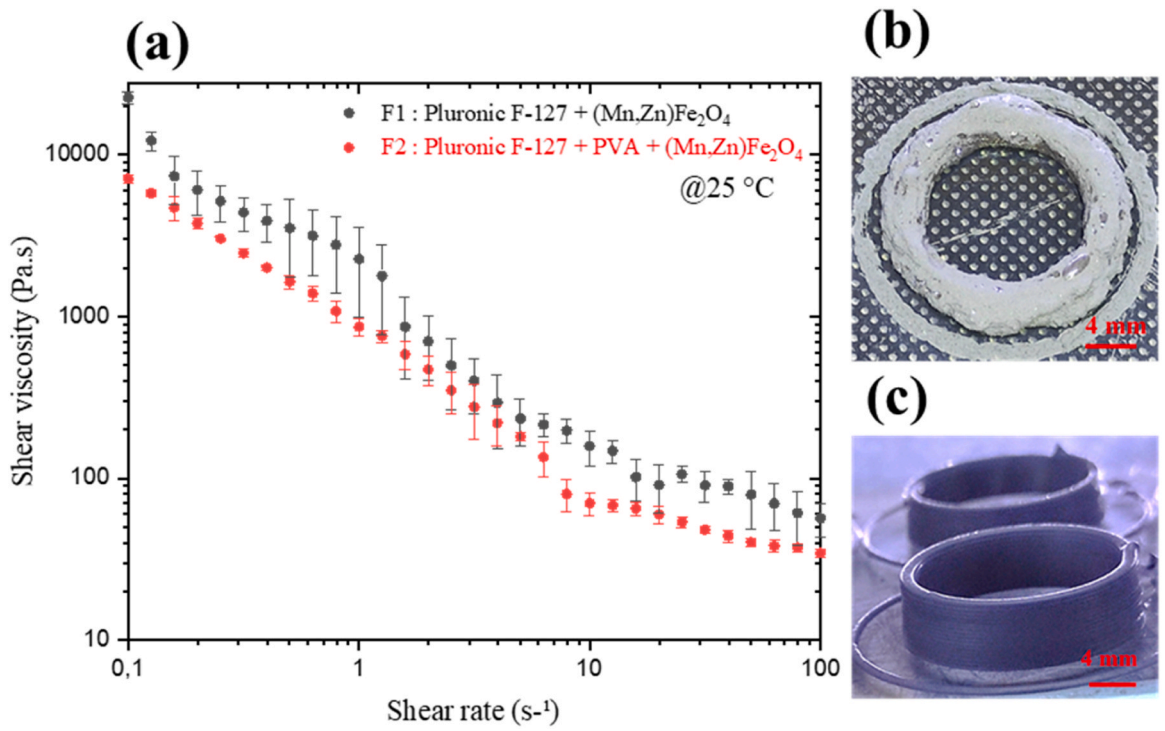

Fig. 3. (a) Variation in the viscosity of the two pastes F#1 and F#2 studied as a function of the shear rate and photograph of printed samples with (b) F#1 and (c) F#2.

increases. However, The F#1 formulation exhibits a high viscosity of 2270 Pa·s at a shear rate of 1 s^{-1}, due to the gelling of Pluronic F-127, occurring around 18 °C [23]. In contrast, the viscosity of formulation F#2, prepared using two binders, PVA and Pluronic F-127 [27], is lower than that of formulation F#1, reaching a value of 864 Pa·s at a shear rate of 1 s^{-1}.

The rheofluidic character suggests the possibility of producing geometries with less layer collapse or sagging during paste deposition by the print heads. The high viscosity of F#1 result in the printing of inhomogeneous filaments as shown in Fig. 3b, which can lead to low green density, lower post-sinter density and therefore reduced magnetic performances. The viscosity level of the second feedstock F#2 offers promising prospects for facilitating extrusion of the 82 wt% (48 vol%) filled paste. In particular, Fig. 3c illustrates the absence of inhomogeneous filaments on a torus printed from the F#2 formulation. In the following, only results obtained with the formulation F#2 will be presented.

3.2. Geometrical stability upon 3D printing

Fig. 4 shows microscopic observations of printed core with a focus on the filaments stacks for two different substrate temperature. The outer surface of the toroid printed at a temperature of 22 °C (Fig. 4a) exhibits extruded filaments that tend to sag and deform, causing distortion of the printed layers: under this condition, the first four layers are no more distinguishable resulting in a poorly controlled geometry.

The second extrusion attempt was carried out at a substrate temperature of 30 °C. The filaments shown in Fig. 4b reveal an improved construction of the printed layers, with less deformation of the extruded filaments as the print head moved along X, Y and Z. The first four printed layers are clearly discernible in Fig. 4b. The extrusion was optimised at a

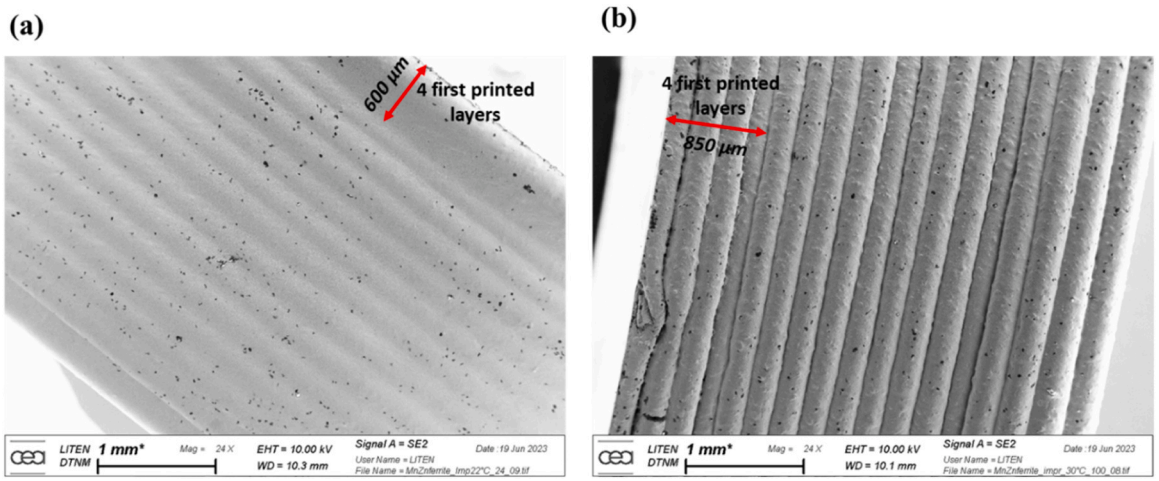

Fig. 4. Scanning electron microscopy images (secondary electron mode) Showing the stacking of the printed filaments obtained for two different substrate temperatures, at 22 °C, and (b) at 30 °C.

print speed of 2 mm.s^{-1} to give good precision when building up the layers. The height of the first layer was set at 0.2 mm, while the next 16 layers were configured with a height of 0.3 mm each.

The F#2 formulation is characterised by a high fluidity at room temperature (22 °C), which is detrimental for the printing of parts with thin walls. However, the viscosity was found to rise rapidly with the temperature. Actually, printing at a substrate temperature of 30 °C contributes to a change in the viscosity of the paste, leading to a transition in the hydrogel material in which the powder is dispersed. This transition, also known as Sol-Gel, corresponds to the formation of a network of micelles made up of Pluronic F-127. The formation of these micelles is responsible for the appearance of gelation in the Pluronic F-127 hydrogel [23], leading to a significant increase in the viscosity of the strands deposited on the support. In the rest of the study, it was decided to print cores at a substrate temperature of 30 °C in order to avoid the problem arising from poorly controlled dimensions, especially when measuring total magnetic losses and permeability.

Fig. 5 shows two SEM images of two cores printed and sintered at 1160 °C with a 4-hour stage. Fig. 5(a) shows an observation of the printed layers of a core based on the F#2 formulation that had not been degassed during formulation preparation, and Fig. 5(b) shows an image of the printed layers of a core based on the degassed F#2 paste. These two images provide a mean of evaluating the density quality of the printed parts by characterising the macroporosity repartition. By comparing the two images, the core printed from a non-degassed paste exhibits large pores (with sizes ranging from 30 μm to 200 μm) and a much higher surface fraction of macroporosity, than a core printed from the same paste that has undergone an additional preparation step. These SEM images show that the morphology of the macroporosity has a quasi-spherical shape. These results indicate the importance of introducing a degassing step into the paste preparation stages in order to eliminate as far as possible the air bubbles trapped in the paste.

Table 2 shows the values for green density (geometrical density) and wall thickness for printed cores and reference cores. These results are required to verify the desired dimensions of the printed parts in order to produce printed parts with low wall thicknesses. The Table 2 shows that the walls of the printed cores have a low dimensional tolerance when a series of magnetic cores are printed, demonstrating good dimensional control during the printing process. The green density obtained on the printed parts corresponds to a relative density of around 55 %, while the green density of the reference part corresponds to a relative density of around 56 %. This density is a geometric density determined from the mass and dimensions of the green part. The Archimedes technique based on ethanol cannot be used for this measurement since the part is dissolved in ethanol when the wet and immersed masses are measured, which means that open and closed porosity cannot be quantified at that step by such.

Table 2
Green density and wall thickness of non-debinded cores obtained using the Std. and material extrusion processes.

	Printed core (T-AM)	Compacted core (T-Std.)
Green density (g/cm^3)	2.80 ± 0.04	2.89 ± 0.04
Wall thickness (mm)	1.77 ± 0.03	3.96 ± 0.04

3.3. Thermal debinding

The Mn-C phase diagram highlights the possible formation of some secondary phases during heat treatment at temperatures around 420 °C [28]. Upon the debinding of printed parts, some carbon residues can combine with the manganese present in the ferrite, giving rise to compounds such as Mn_5C_2 and Mn_7C_3. The carbide manganese phases do not contribute to the magnetism of the system but do affect the permeability of the sintered cores. For this reason, it is preferable to maintain the temperature below 400 °C during debinding.

Fig. 6 shows the thermogravimetric analysis (TGA) carried out on a sample of a printed part (Fig. 1d) which was previously air-dried for 24 hours meaning that the percentage of solvent (DI water), evaporated almost completely, is not included in the mass of the sample analyzed by TGA.

This analysis confirms the mass percentage of the powder and helps to define the decomposition temperatures of each organic constituent. Analysing the TGA curve, the first component to degrade was the dispersant, followed by the binder, made up of two polymers, PVA and Pluronic F-127. The latter two degrade completely as the temperature approaches 400 °C. These findings, based on TGA, suggest that a debinding temperature of 400 °C should be set.

In addition, in order to quantify the paste loading rate after water removal, we followed [13] which has introduced the SLED (solid loading excluding diluent) as a figure of merit for densification. It is expressed in Eq. (1) using the values in Table 1.

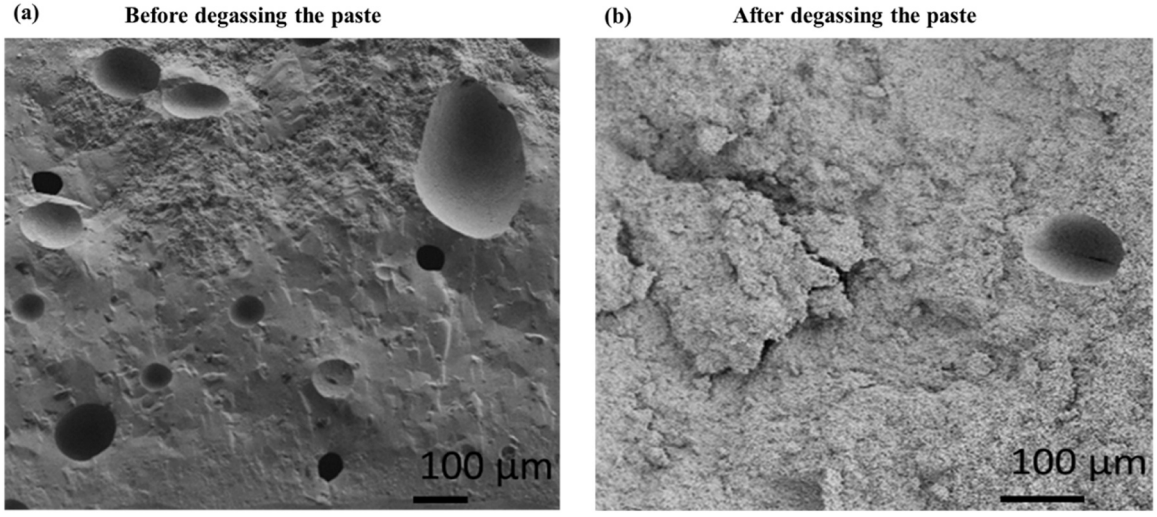

Fig. 5. Scanning electron microscopy images (secondary electron mode) illustrating the macroporosity in the cores printed from F#2 paste, (a) non-degassed and (b) degassed.

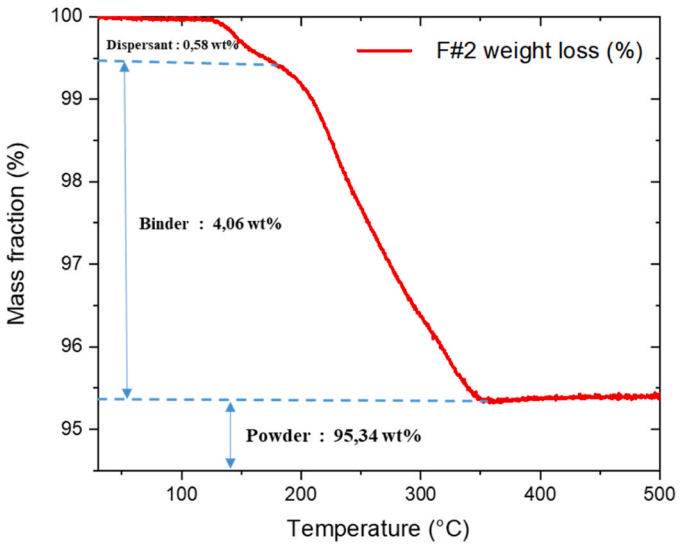

Fig. 6. Thermogravimetric analysis carried out on a toroid sample printed from formulation F#2 and then dried in air.

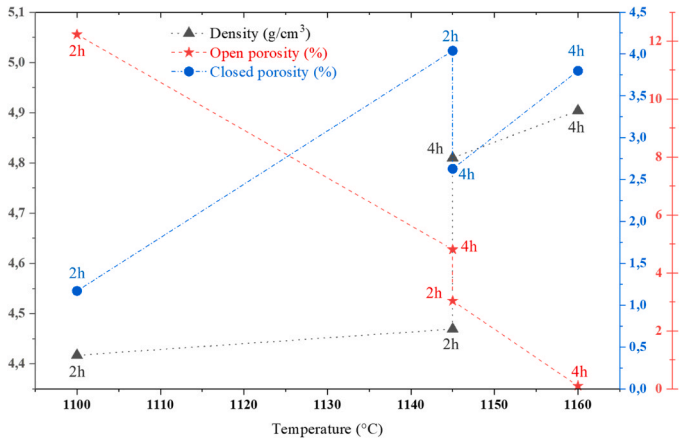

Fig. 8. Density, closed porosity and open porosity as a function of sintering temperature of cores prepared by standard process for different combinations of holding temperature and time.

conditions, different densification tests have been performed on Std. samples with several combinations of holding temperature and duration. The thermal treatment are carried out under an oxygen partial pressure of 0.7 % required for MnZn ferrites densification [31,32]. The final density and open porosity values have been determined after sintering for the different holding temperature and time used. The obtained results are plotted on the Fig. 8 versus the sintering temperature. From these data, the optimum cycle was deduced, aimed at minimising open porosity while maximising the final density (theoretical powder density 5.1 g/cm^3). The optimum temperature was set at 1160 °C for a 4-h stage duration.

Fig. 9 shows an image of the compacted cores (T-Std.) and the printed cores (T-AM) that were sintered simultaneously at the selected sintering temperature (1160 °C-4 h). The shrinkage observed in the printed parts and the reference parts was approximately 16 % along the

$$SLED = \frac{W_{Powder}}{W_{Powder} + W_{PVA\ +\ PluronicF-127} + W_{Disperbyk111}} = \frac{72.16}{72.16 + 3.08 + 0.44} \approx 95.34\ \% \quad (1)$$

The value obtained here is above 94 %, in a range that allows maximum densities to be achieved after sintering.

3.4. Densification

The dilatometry curve plotted in Fig. 7 shows that the densification of the ferrite starts around 900 °C and is complete at 1160 °C. However, since the dilatometer analysis is carried out in air, it does not provide all the information needed to define the sintering cycle. This is mainly due to the requirement to sinter (Mn,Zn)Fe_2O_4 ferrite in a controlled atmosphere [29]. For different sintering cycle conditions, this atmosphere makes it possible to control the oxidation state of the divalent and trivalent ions [30]. In order to determine the optimal sintering

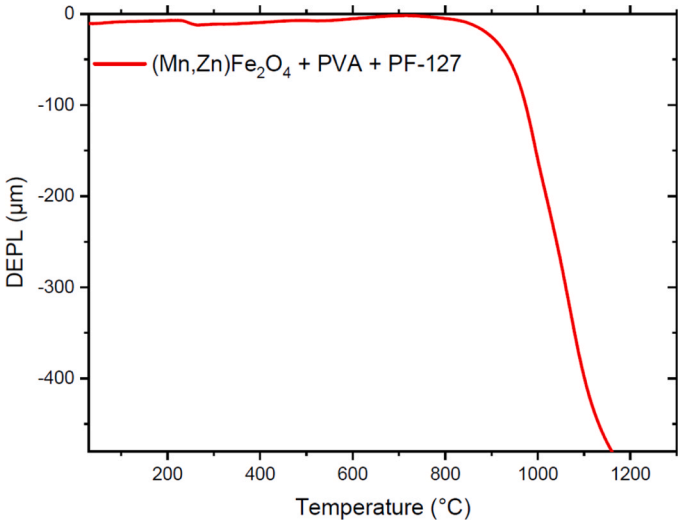

Fig. 7. Evolution of axial shrinkage measured by dilatometry as a function of temperature for a pellet prepared with the formulation F#2.

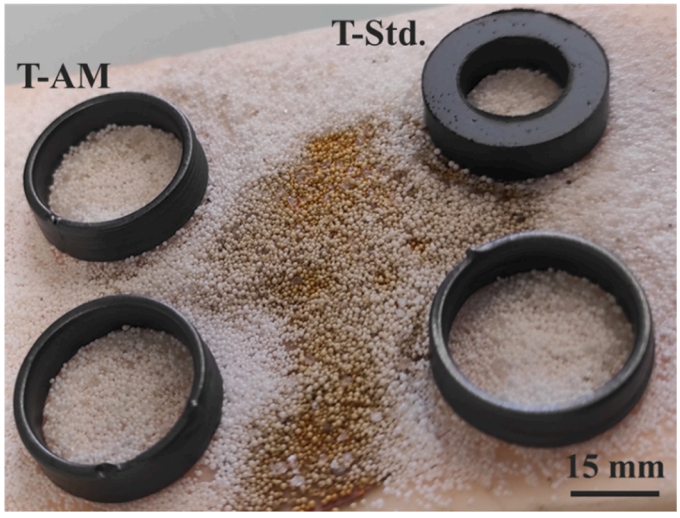

Fig. 9. Photograph of the printed cores (T-AM) and reference cores (T-Std.) sintered simultaneously at 1160 °C with a 4-hour stage.

horizontal axis (diameter). However, along the vertical axis (height), the shrinkage was 18 and 19 % in the printed (T-AM) and reference (T-Std.) parts respectively. Shrinkage in both parts along the horizontal axis was similar. However, in the vertical axis, the shrinkage was very marked in the reference part compared with the printed part. In both parts, the shrinkage was anisotropic, with a more significant shrinkage along the vertical axis (height) compared to the horizontal axis (diameter).

In the case of the reference part, this was due to uniaxial compaction along the vertical axis, which favours welding between particles during densification mechanisms. For the printed part, the shrinkage was slightly anisotropic with regard to the horizontal axis. This is due to the slight stress applied by the nozzle during the deposition of the extruded filaments to prevent the part from collapsing during printing. There may also be gravitational effects in both cases that favour increased shrinkage along the vertical axis.

Table 3 shows a comparison of the density, open porosity and closed porosity of the printed and reference cores after sintering at 1160 °C for 4 hours. The printed core has a lower density and higher porosity (open and closed) than the reference core. This difference is due to differences in the manufacturing processes. In the standard process, densification consists of two stages: compacting the particles under pressure, followed by densification by heat treatment (sintering). However, printed parts do not undergo a compaction stage beforehand. They are simply formed by depositing layers to form a core, and densified only by heat treatment (sintering). These printed cores may still have residual porosities caused by imprisoned air and the absence of compaction stress during construction of the part.

X-ray diffraction measurements are shown in Fig. 10 and confirm the presence of the diffraction peaks that characterise the spinel phase of the Mn-Zn ferrite. However, for sintering temperatures of 1100 °C and 1145 °C, a weak diffraction peak characterises the presence of traces of ZnO zinc oxide phase, the intensity of this ZnO phase diffraction peak decreases and becomes even weaker in cores sintered at 1160 °C. These diffraction results confirm the absence of other parasitic manganese or carbon phases mentioned above. Furthermore, as expected, the sintering atmosphere chosen for sintering MnZn ferrite-based cores prevents the formation of the Fe_2O_3 hematite phase.

3.5. Microstructural analysis of sintered cores

Observation of the microstructure is useful to understand the link between magnetic properties and the type of microstructure obtained. The result of processing SEM images by ImageJ software leads to an average grain size of $D_g = 4.00 \pm 1.70$ μm in Fig. 11a of a reference torus. The same analysis was carried out on a 3D printed toroid (T-AM) in Fig. 11b shows a grain size with values of $D_g = 3.50 \pm 1.50$ μm, which is slightly smaller than the size found in the standard toroid (T-Std.).

In reference [33], it was assessed, based on neutron depolarization experiments, that the critical size at which the grain passes from a monodomain to a bidomain was around 4 μm in polycrystalline (Mn,Zn) Fe_2O_4 ferrite. Here, the measured distribution lies on either side of the critical size of around 4 μm which corresponds to the transition between monodomain and bidomain grains in polycrystalline (Mn,Zn)Fe_2O_4 ferrite.

Table 3
Density and porosity of sintered parts (3D printed and reference) at 1160 °C during a 4-hour stage.

	Printed core (T-AM)	Compacted core (T-Std.)
Density (g/cm^3)	4.64 ± 0.01	4.90 ± 0.01
Closed Porosity (%)	6.20 ± 0.20	3.80 ± 0.10
Open Porosity (%)	2.80 ± 0.20	0.10 ± 0.05

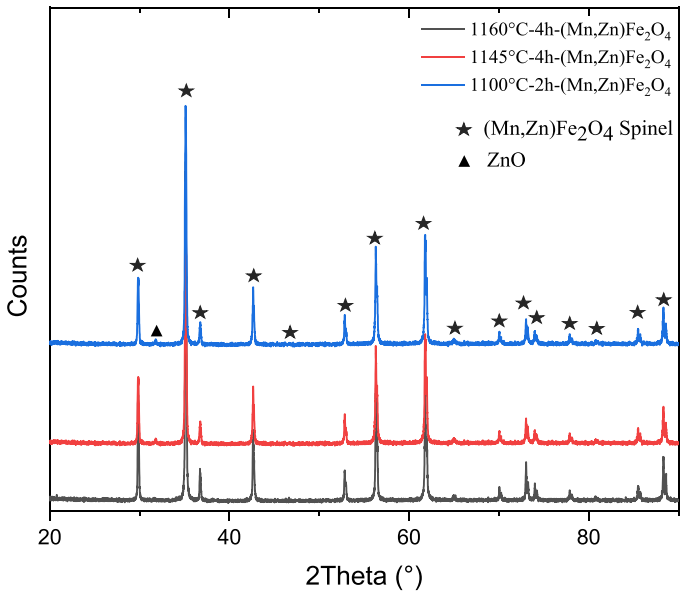

Fig. 10. X-ray patterns (XRD) of MnZn ferrite from printed and sintered core samples at different temperatures.

3.6. Magnetic properties of sintered cores

3.6.1. Permeability and hysteresis cycles at low frequency

The values of relative permeability μ_r at room temperature measured on both samples are given in Table 4. Within the frequency range of [10^4-10^6 Hz], the values of the relative permeability of AM core is slightly lower (1250) than for the Std. core (1300).

Fig. 12 illustrates the hysteresis cycle obtained for the same materials for two frequencies (1 and 10 kHz). It is worth noting that the hysteresis cycle, when changing frequency from 1 to 10 kHz for the same sample, keeps practically the same cycle area. These measurements give access to three magnetic properties: saturation polarization (J_s), remanent induction (B_r) and coercive field (H_c) which are given in Table 4 for a frequency of 1 kHz. The saturation polarization of the T-AM toroid is 0.45 T, slightly lower than that of the T-Std. toroid (0.47 T). In the same time, the coercive field strength of the T-AM toroid is 58 A/m, higher than that of the T-Std. toroid $H_c = 44$ A/m. This variation in magnetic properties is attributed to the difference in the residual porosity: the AM sample has a relative density of 91 % with a closed porosity of 6.20 % and an open porosity of around 3 %, whereas the reference part has a relative density of 96 % with a closed porosity of 3.80 % and a low open porosity (< 1 %). After normalization to the density (d), the values reported in Table 4 are very close.

The impact of closed porosity is to increase the energy required to achieve saturation magnetisation. Closed porosity acts as a barrier to the movement of magnetic domain walls, reducing the magnetic permeability.

3.6.2. Core loss

Core loss values measured at constant induction value (50 mT) are plotted in Fig. 13a within the frequency range of 200–1000 kHz. For frequencies below 300 kHz, the losses of the printed (AM) and the standard (Std.) sample are comparable. However, as the frequency rises above 300 kHz, the total magnetic loss levels become greater in the Std. sample.

Fig. 13b shows the evolution of core losses as a function of induction at 1 MHz. This measurement shows comparable loss behavior for induction values below 60 mT. Above 70 mT, core losses become more significant in the Std. toroid.

In (Mn,Zn)Fe_2O_4 ferrites [6,31,34], it is generally considered that total losses can be broken down into three terms: hysteresis losses P_{hy},

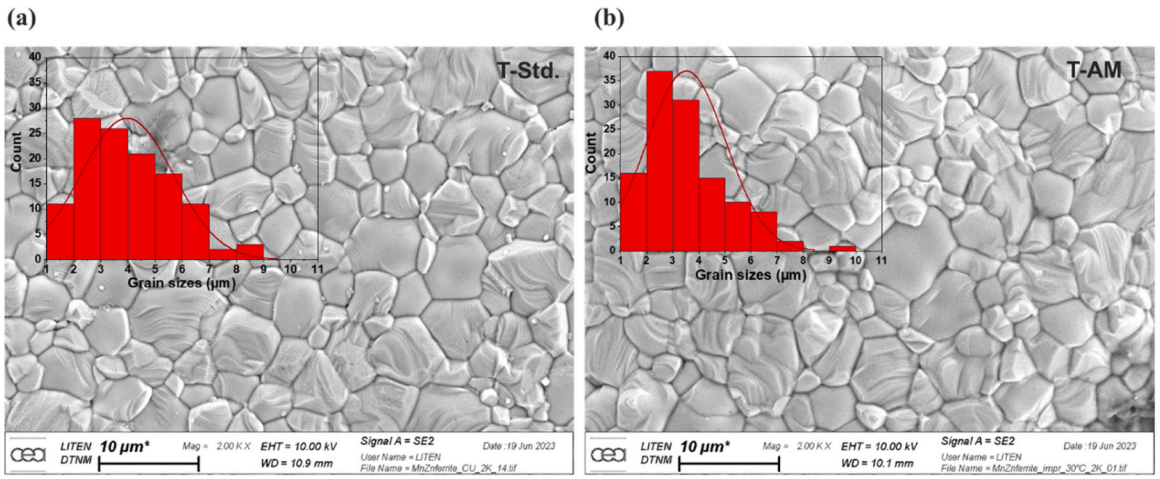

Fig. 11. Scanning electron microscopy images (secondary electron mode), (a) Microstructure of a (Mn,Zn)Fe_2O_4 ferrite toroid produced by standard process (T-Std.) sintered at 1160 °C in a controlled atmosphere, and (b) Microstructure of a printed toroid (T-AM) sintered under the same conditions.

Table 4
Magnetic properties for T-AM and T-Std..

Without normalization to density					After normalization to density		
Sample	Permeability μ (10^4 to 10^6 Hz)	J_s (T) @1 kHz	B_r (T) @1 kHz	H_c (A/m) @1 kHz	density d (g/cm^3)	μ/d (cm^3/g)	J_s/d (T.cm^3/g)
AM sample	1250	0.45	0.28	58	4.64	269	0.097
Std. sample	1300	0.47	0.26	44	4.89	266	0.096

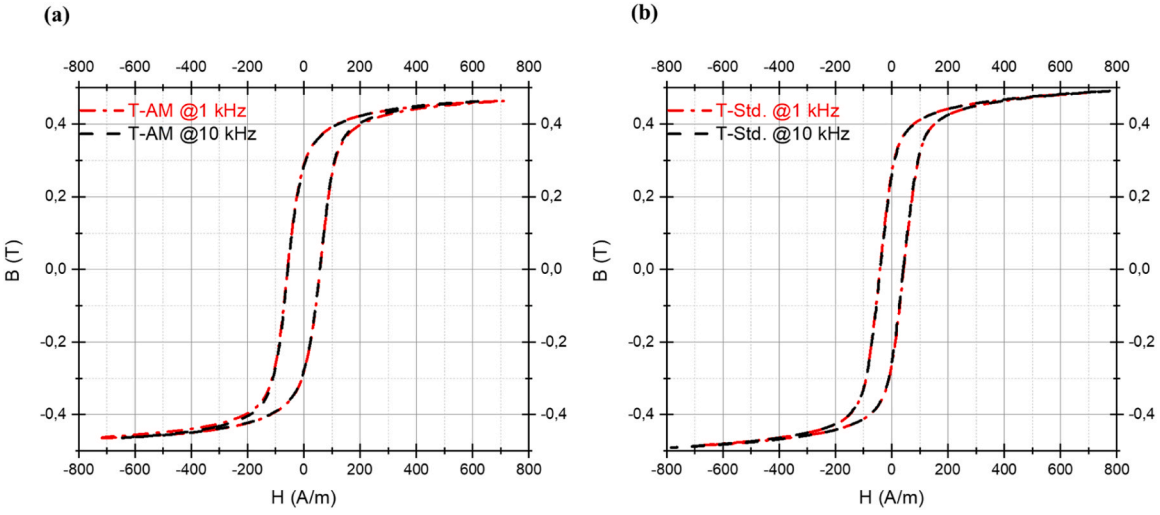

Fig. 12. (a) Hysteresis cycles for a 3D printed toroid (T-AM), and (b) for a conventional processed toroid (T-Std.) at 1 and 10 kHz.

eddy current losses P_{ec} and excess losses P_{ex}.

$$P_{hy} = a * K(T) * B^3 * f \quad (2)$$

$$P_{ec} = b * \frac{D_g^2}{\rho(T)} * B^2 * f^2 \quad (3)$$

$$P_{ex} = c * B^m * f^n \quad (4)$$

With a, b and c constants, K the anisotropy energy which generally decreases with temperature, D_g the grain size, m and n constants dependent on the material and ρ the electrical resistivity which also depends on temperature. Each of these contributions varies as a function of frequency according to a power law with a different exponent value. This feature allows to adjust the experimental data obtained for a given induction value in order to determine the importance of each of the three contributions.

For constant induction and temperature values, the previous core loss laws can be expressed with a simplified expression from which the fitting of the experimental data plotted in Fig. 13a has been performed:

$$P_c = K_{hy}f + K_{ec}f^2 + K_{ex}f^n \quad (5)$$

Table 5 summarizes the values of the fitted parameters obtained.

It has been found that the last term in Eq. (5) (excess loss) represents, for both samples, less than 10 % of the total core loss within the whole studied frequency range, meaning that the losses are dominated by the hysteresis loss and, in a less extent, by the classical eddy current

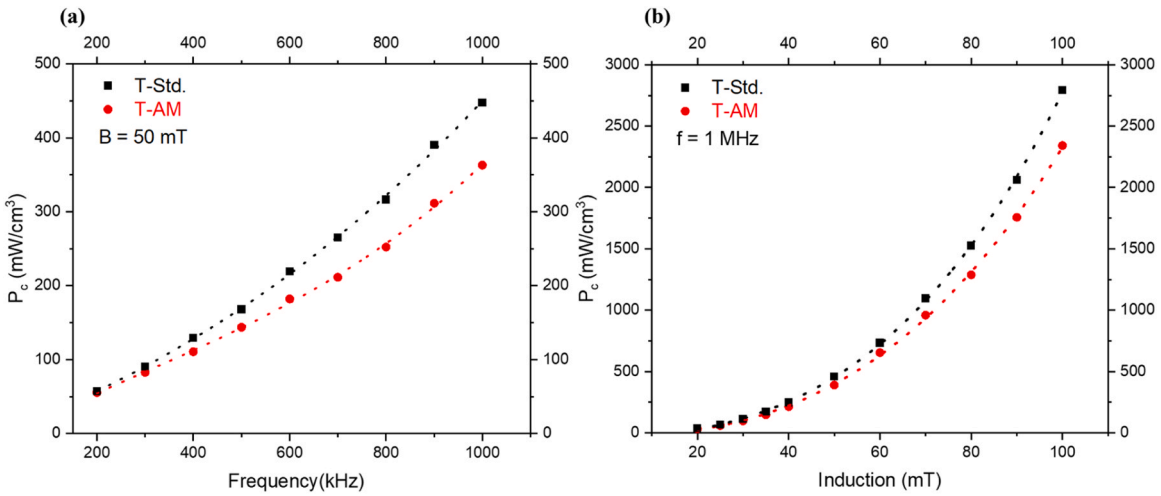

Fig. 13. (a) Evolution of total magnetic losses as a function of frequency determined for 3D printed (T-AM) and standard processed (T-Std.) toroids, and (b) as a function of magnetic induction at 25 °C.

Table 5
Values of the fitted parameters used in Eq. (5) for frequency values in kHz and P_c in W.m^{-3} and for an induction B = 50 mT. The mean absolute error (MAE) of the fit was 1.2 and 3.2 % for Standard and AM samples respectively.

	K_{hy} (W.m^{-3}.kHz^{-1})	K_{ec} (W.m^{-3}.kHz^{-2})	K_{ex} (W.m^{-3}.kHz^{-n})	n
AM sample	232	6.84 10^{-2}	5.21 10^{-4}	2.68
Std. sample	250	1.54 10^{-1}	1.53 10^{-4}	2.83

contribution. Fig. 14 shows the share of hysteresis losses, eddy current losses and excess losses in both samples. For the printed sample, the hysteresis loss and eddy current constitute respectively 84 % and 5 % of the total loss at 200 kHz. At 1 MHz, the weights of the two terms are shifted to 64 % and 19 %. For the Std. sample, the repartition of the core loss terms is 87 % (hysteresis) and 11 % (eddy current) at 200 kHz, whereas, at 1 MHz, the corresponding figures are 56 % and 34 %. It is worth noting that the hysteresis term K_{hy} is slightly low in the printed sample whereas the eddy current parameter, K_{ec}, is about two times higher for the Std. sample compared to the printed one.

4. Discussion

In this section, the dependence of the eddy current loss term on the samples characteristics is investigated. The calculation method of this loss term in MnZn ferrite toroidal cores, established by Furuya et al. [35] and Kawano et al. [36], has been considered. This approach aims at computing a realistic distribution of the eddy current and subsequent loss in polycrystalline MnZn samples. Basically, the model allows studying the non-homogeneous penetration of the magnetic field, related to the skin effect, which leads to a dimensional dependence of the core loss. Moreover, the model also considers the influence of some microstructural parameters, notably the differences of dielectric and conductive properties between the grain boundary and the grain phases, on the evolution of the eddy current with increasing frequency. The grains with a size D_g, made of the MnZn spinel phase, are assumed to have a high conductivity σ_1 and to be perfectly covered by a high resistivity oxide layer with a thickness δ. This thin phase exhibits a dielectric permittivity ε and a low conductivity $\sigma_2 << \sigma_1$ which allows the limitation of eddy current across the grain boundary. At the microscopic scale, the equivalent electrical circuit of a grain surrounded by the grain boundary layer is described by a resistance (grain) in series with a couple made of a resistance and a capacitor in parallel (grain

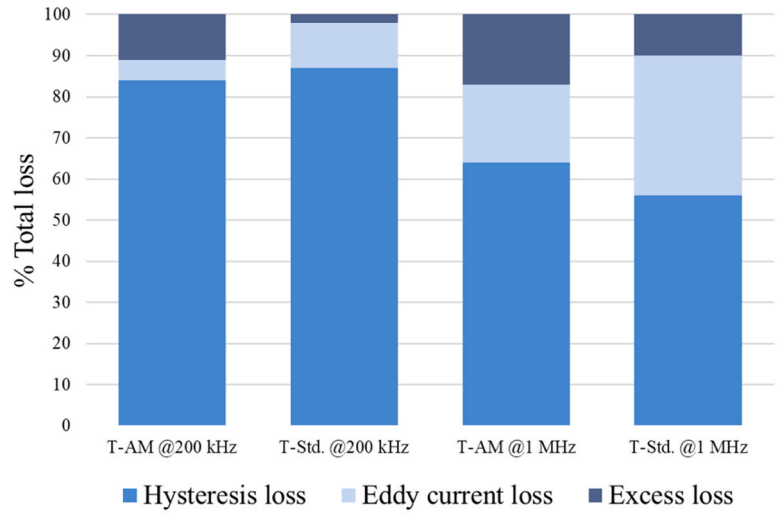

Fig. 14. Core loss decomposition at 50 mT and 25 °C for both standard and AM sample as determine at 200 kHz and 1 MHz.

Table 6
Values of physical parameters used in the calculation of the eddy current loss.

Name	Symbol	Value
Conductivity in grains	σ_1	1100 S/m [37]
Conductivity in grain boundary layer	σ_2	3.5 10^{-4} S/m [37]
Grain size	D_g	Std.: 4. 10^{-6} m [this work] AM: 3.5 10^{-6} m [this work]
Grain boundary layer thickness	δ	0.9 nm [37]
Dielectric constant	$\varepsilon/\varepsilon_0$	7 [37]
Permeability	μ/μ_0	1300 [this work]
Excess loss coefficient	C_β	10^{-12} [this work]

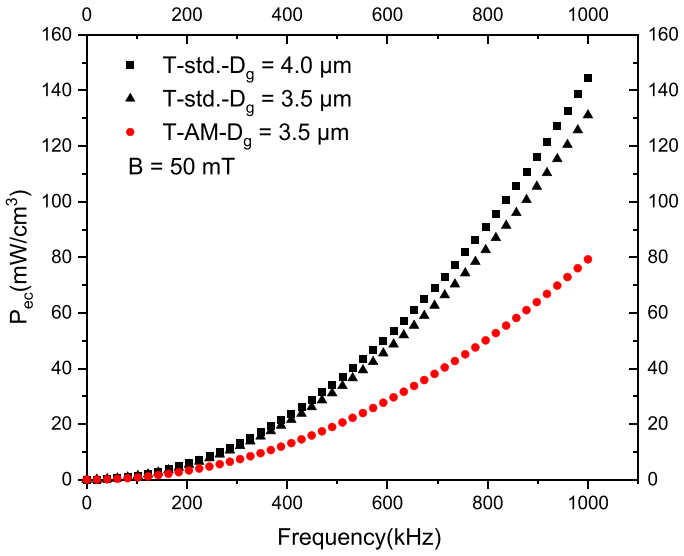

Fig. 15. Eddy current loss calculated in the (Mn,Zn)Fe_2O_4 toroid samples with the model parameters listed in the Table 6.

boundary). Rimal et al. [37] proposed to solve the Maxwell equations in such a composite medium owing to a Finite Difference scheme. This last approach has been implemented in this work considering the magneto-harmonic approximation and adding the excess loss term introduced by Furuya et al. [35] The value of the parameter C_β that accounts for this last contribution has been adjusted in this work in order to obtain a contribution of excess loss lower than 10 % of the total loss (for B = 50 mT). It is worth noting that the model does not consider the hysteresis loss and the wall displacement contribution to the total loss.

The Table 6 provides the values of the physical parameters used in the calculation of the eddy current loss. The other parameters are the dimensions of the toroid samples, the 3D printed core being thinner (1.47 ± 0.04 mm) compared to the Std. sample (3.30 ± 0.05 mm, see Table A1).

The eddy current loss computed with the model for the two sample geometries and for an induction value of 50 mT are plotted on Fig. 15. The core loss for the Std. sample is found to be higher than for the printed core, by a factor which is close to 2 up to 600 KHz, in good agreement with the experimental results. The gap between the grain sizes of the two samples, considered separately, accounts only for 10 % of the core loss variation. The difference between samples loss is mainly due to the impact of the torus thickness on the eddy current repartition. For higher frequencies, the ratio of the calculated core loss values is found to be larger than 2. This is due to the onset of the influence of the dimensional resonance that is expected to occur, according to the current values of the model parameters, at 3 MHz for the large core and 5 MHz for the thin one. Disregarding the dimensional effects, it is worth noting that the 3D printed and conventionally manufactured MnZn cores are expected to provide similar magnetic performances. Thus confirming the usefulness of the 3D printing process route developed here.

5. Conclusion

In this work, a highly loaded powder formulation (82 wt%) demonstrated rheofluidic behaviour, enabling the paste to be extruded through 1 mm metal nozzles during robocasting. Optimization of the printing parameters, carried out at a substrate temperature of 30 °C, resulted in toroidal samples with straight geometries, resistant to sagging when extruded filaments were superimposed during the building. The thermal cycle and the atmosphere (1160 °C - 4 h – 0.7 % O_2) chosen for sintering the printed cores favored the formation of the spinel magnetic phase of the ferrimagnetic material (Mn,Zn)Fe_2O_4.

Measurement of the permeability and core loss showed that the performances of the parts manufactured by material extrusion are equivalent to the samples made by the conventional shaping process, with the same MnZn powder. However, when the frequency becomes higher than 300 kHz, the losses in the printed parts become greater than in the reference part, this difference is mainly due to eddy current losses, which are particularly significant in reference samples with larger effective areas. This result encourages the use of this innovative technique for the implementation of applications based on magnetic cores with complex geometries. More particularly, it is worth noting that the 3D printing by material extrusion allows designing ferrite components with thin wall dimensions (i.e. the same order than the extruded filaments) that could avoid the detrimental effects of the dimensional resonance for high frequency operation due to eddy current.

CRediT authorship contribution statement

A. Zekhnini: Methodology, Investigation, Data curation, Writing - original draft, Writing - review and editing, Conceptualization. **G. Delette:** Methodology, Data curation, Software, Writing - original draft, Supervision, Validation. **A.L. Adenot-Engelvin:** Methodology, Investigation, Writing - review and editing, Supervision, Validation. **O. Isnard:** Methodology, Investigation, Writing- Reviewing and Editing, Supervision, Validation.

Declaration of Competing Interest

The authors declare that they have no known competing financial interests or personal relationships that could have appeared to influence the work reported in this paper.

Data Availability

Data will be made available on request.

Acknowledgements

The authors would like to thank Theo Richard and Karine Escudié for the hysteresismeter characterizations at CEA Le Ripault.

Appendix I. Extraction of relative permeability from impedance measurement

The impedance links the voltage U and current I signals applied to the terminals of the wound toroid studied here over a frequency range from 10 kHz to 1 MHz.

$$\underline{Z}(\omega) = \frac{\underline{U}}{\underline{I}} \tag{A1}$$

The permeability values are deduced from measured complex impedance, assuming linear behavior for the low amplitudes of the harmonic signals used. The currents I and voltages U are related respectively to the field H and magnetic induction B in the toroid by the following expressions, derived from Ampère's and Lenz's laws:

$$\underline{H}(\omega) = \frac{N\underline{I}(\omega)}{l_{eff}} \tag{A2}$$

$$\underline{B}(\omega) = \frac{\underline{U}(\omega)}{j\omega NA_{eff}} \tag{A3}$$

The complex permeability is defined by:

$$\underline{\mu} = \frac{\underline{B}}{\underline{H}} = \frac{|B|}{|H|} e^{-j\varphi} = \mu' - j\mu'' \tag{A4}$$

By transferring expressions Eqs. (A2) and (A3) to relations Eq. (A1) and then Eq. (A4), we obtain the following relation which allows us to identify the μ' and μ'' components with the impedance values:

$$\underline{Z}(\omega) = \omega N^2 \frac{A_{eff}}{l_{eff}} \mu'' + j\omega N^2 \frac{A_{eff}}{l_{eff}} \mu' \tag{A5}$$

To carry out this measurement, two windings were produced, a primary coil and a secondary coil. Due to the presence of Joule effect losses in the winding on the toroid, two successive measurements were carried out to separate the contributions from the wires and those from the toroid itself. To do this, we define an open-circuit impedance (Z_{OC}) and a short-circuit impedance (Z_{SC}), which we can express neglecting the high frequency capacitive effects as follows:

$$\underline{Z_{OC}}(\omega) = R_{OC}(\omega) + j\omega L_{OC}(\omega) \tag{A6}$$

$$\underline{Z_{SC}}(\omega) = R_{SC}(\omega) + j\omega L_{SC}(\omega) \tag{A7}$$

The impedance after compensation is given by: $Z_{comp} = Z_{OC} - Z_{SC}$ Eq. (A8)

The effective length l_{eff} (average length of the magnetic circuit) and the effective area A_{eff} (cross-sectional area of the magnetic circuit) are parameters, which take into account the inhomogeneity of the magnetic flux throughout the cross-section of the torus:

$$A_{eff} = \frac{h}{2} \frac{\ln\left(\left(\frac{D_o}{D_i}\right)^2\right)}{\frac{1}{D_i} - \frac{1}{D_o}} \tag{A9}$$

$$l_{eff} = \frac{\pi \ln\left(\frac{D_o}{D_i}\right)}{\frac{1}{D_i} - \frac{1}{D_o}} \tag{A10}$$

Where:- L_{OC}, L_{SC} are the inductances measured in open circuit and short circuit respectively.- R_{OC}, R_{SC} represent the open-circuit and short-circuit resistances respectively.- D_o is the outside diameter, D_i the inside diameter and h the height of the toroid.- N is the number of winding turns

Table A1 shows the dimensions of the cores used for the permeability measurements.

Table A1
Dimensions of sintered cores obtained using the Std. and material extrusion processes.

Sample type	D_o (mm)	D_i (mm)	H (mm)
T-AM	16.30	13.35	4.35
T-Std.	15.40	8.90	4.15

References

[1] J. Smit and H.P.J. Wijn, Ferrites. The Netherlands: Philips Technical Library, Eindhoven, 1959.

[2] P. Thakur, D. Chahar, S. Taneja, N. Bhalla, A. Thakur, A review on MnZn ferrites: synthesis, characterization and applications, Ceram. Int. 46 (10) (2020) 15740–15763, https://doi.org/10.1016/j.ceramint.2020.03.287.

[3] G. Delette, U. Soupremanien, S. Loudot, Thermal Management Design of Transformers for Dual Active Bridge Power Converters, IEEE Trans. Power Electron. 37 (7) (2022) 8301–8309, https://doi.org/10.1109/TPEL.2022.3152692.

[4] R. Hosseini, R. Cuzner, A High Frequency Power Transformer for isolated bidirectional DC-DC Converter used for MVDC Collection System in Wind Farmser, 2019 8th Int. Conf. Renew. Energy Res. Appl. (ICRERA) (2019) 593–598, https://doi.org/10.1109/ICRERA47325.2019.8996566.

[5] P. Andalib, Y. Chen, V.G. Harris, Concurrent core loss suppression and high permeability by introduction of highly insulating intergranular magnetic inclusions to MnZn Ferrite, IEEE Magn. Lett. 9 (2018) 1–5, https://doi.org/10.1109/LMAG.2017.2771391.

[6] W.H. Jeong, Y.H. Han, B.M. Song, Effects of grain size on the residual loss of Mn–Zn ferrites, J. Appl. Phys. 91 (10) (2002) 7619–7621, https://doi.org/10.1063/1.1447506.

[7] S. Takahashi, S. Ogasawara, M. Takemoto, K. Orikawa, M. Tamate, Experimental evaluation of the relationship between dimensional dependencies of MnZn ferrites and filter inductor impedances, Electr. Eng. Jpn. 214 (2) (2021) e23302, https://doi.org/10.1002/eej.23302.

[8] D. Xu, K. Ngo, Optimal constant-flux-inductor design for a 5 kW boost converter, 2013 Twenty-Eighth Annu. IEEE Appl. Power Electron. Conf. Expo. (APEC) (2013) 2436–2443, https://doi.org/10.1109/APEC.2013.6520637.

[9] R.S. Yang, A.J. Hanson, B.A. Reese, C.R. Sullivan, D.J. Perreault, A low-loss inductor structure and design guidelines for high-frequency applications, IEEE

Trans. Power Electron. 34 (10) (2019) 9993–10005, https://doi.org/10.1109/TPEL.2019.2892397.
[10] X. Wei, Y. Pan, Z. Chen, 3D printing of NiZn ferrite architectures with high magnetic performance for efficient magnetic separation, J. Eur. Ceram. Soc. 42 (4) (2022) 1522–1529, https://doi.org/10.1016/j.jeurceramsoc.2021.11.052.
[11] Y. Hu, et al., Preparation of Mn–Zn ferrite ceramic using stereolithography 3D printing technology, Ceram. Int. 48 (5) (2022) 6923–6932, https://doi.org/10.1016/j.ceramint.2021.11.248.
[12] T. An, K.-T. Hwang, J.-H. Kim, J. Kim, Extrusion-based 3D direct ink writing of NiZn-ferrite structures with viscoelastic ceramic suspension, Ceram. Int. 46 (5) (2020) 6469–6476, https://doi.org/10.1016/j.ceramint.2019.11.127.
[13] L. Liu, K.D.T. Ngo, G.-Q. Lu, Guideline for paste extrusion 3D printing of slump-free ferrite inductor cores, Ceram. Int. 47 (4) (2021) 5803–5811, https://doi.org/10.1016/j.ceramint.2020.10.167.
[14] Z. Luo, Q. Yue, X. Li, Y. Zhu, X. Liu, L.A. Fielding, Polymer-assisted 3D printing of inductor cores, ACS Appl. Mater. Interfaces 16 (8) (2024) 10764–10773, https://doi.org/10.1021/acsami.3c18956.
[15] L. Tabard, et al., Robocasting of highly porous ceramics scaffolds with hierarchized porosity, Addit. Manuf. 38 (2021) 101776, https://doi.org/10.1016/j.addma.2020.101776.
[16] S.S.L. Chan, M.L. Sesso, G.V. Franks, Direct ink writing of hierarchical porous alumina-stabilized emulsions: Rheology and printability, J. Am. Ceram. Soc. 103 (10) (2020) 5554–5566, https://doi.org/10.1111/jace.17305.
[17] S.C. Altıparmak, V.A. Yardley, Z. Shi, J. Lin, Extrusion-based additive manufacturing technologies: state of the art and future perspectives, J. Manuf. Process. 83 (2022) 607–636, https://doi.org/10.1016/j.jmapro.2022.09.032.
[18] X. Wei, M.-L. Jin, H. Yang, X.-X. Wang, Y.-Z. Long, Z. Chen, Advances in 3D printing of magnetic materials: Fabrication, properties, and their applications, J. Adv. Ceram. 11 (5) (2022) 665–701, https://doi.org/10.1007/s40145-022-0567-5.
[19] S. Kolli, et al., Process optimization and characterization of dense pure copper parts produced by paste-based 3D micro-extrusion, Addit. Manuf. 73 (2023) 103670, https://doi.org/10.1016/j.addma.2023.103670.
[20] S. Jang, et al., Effect of material extrusion process parameters on filament geometry and inter-filament voids in as-fabricated high solids loaded polymer composites, Addit. Manuf. 47 (2021) 102313, https://doi.org/10.1016/j.addma.2021.102313.
[21] A. Hodaei, et al., Single additive enables 3D printing of highly loaded iron oxide suspensions, ACS Appl. Mater. Interfaces 10 (11) (2018) 9873–9881, https://doi.org/10.1021/acsami.8b00551.
[22] E. Feilden, E.G.-T. Blanca, F. Giuliani, E. Saiz, L. Vandeperre, Robocasting of structural ceramic parts with hydrogel inks, J. Eur. Ceram. Soc. 36 (10) (2016) 2525–2533, https://doi.org/10.1016/j.jeurceramsoc.2016.03.001.
[23] L.C. Pham Trong, M. Djabourov, A. Ponton, Mechanisms of micellization and rheology of PEO–PPO–PEO triblock copolymers with various architectures, J. Colloid Interface Sci. 328 (2) (2008) 278–287, https://doi.org/10.1016/j.jcis.2008.09.029.
[24] W.S. Rasband, ImageJ v1.53 (Version 1.53),. U. S. National Institutes of Health, 1997-2018, ⟨https://imagej.net/ij/⟩.
[25] C.F. Foo, D. Zhang, X. LI, A simple approach for determining core-loss of magnetic materials, J. Magn. Soc. Jpn. 22 (1998) S1_277–S1_27279, https://doi.org/10.3379/jmsjmag.22.S1_277.
[26] U. Soupremanien, J.-S. Ngoua-Teu, P. Sallot, C. Delafosse, G. Delette, Soft ferrite material by powder injection molding process for power electronics, IEEE Trans. Magn. 56 (12) (2020), https://doi.org/10.1109/TMAG.2020.3027248.
[27] M. Bercea, R.N. Darie, L.E. Niță, S. Morariu, Temperature responsive gels based on pluronic F127 and poly(vinyl alcohol), Ind. Eng. Chem. Res. 50 (7) (2011) 4199–4206, https://doi.org/10.1021/ie1024408.
[28] C. Akil and A. Geveci, Optimization of Conditions to Produce Manganese and Iron Carbides from Denizli-Tavas Manganese Ore by Solid State Reduction, 32, Jan. 2008.
[29] F. Monforte, R. Chen, P. Baba, Pressure sintering of MnZn and NiZn ferrites, IEEE Trans. Magn. 7 (3) (1971) 345–350, https://doi.org/10.1109/TMAG.1971.1067093.
[30] P. Perriat, B. Gillot, D. Aymes, Oxidation and reduction reactions in spinel oxides: influence upon some physical properties, pp. C1-46, J. Phys. IV vol. 07 (C1) (Mar. 1997), https://doi.org/10.1051/jp4:1997105.
[31] E.C. Snelling, Soft ferrites Properties and Applications, (Second ed.), Butterwoeth&Co-Publishing. London, 1988.
[32] V. Zaspalis, V. Tsakaloudi, E. Papazoglou, M. Kolenbrander, R. Guenther, P. van der Valk, Development of a new MnZn-Ferrite soft magnetic material for high temperature power applications, J. Electroceram. 13 (1) (2004) 585–591, https://doi.org/10.1007/s10832-004-5162-3.
[33] J. Aarts, I. Shiekah, P.J. van der Zaag, Domain structure in polycrystalline MnZn ferrite imaged by magnetic force microscopy, J. Appl. Phys. 85 (1999) 7302–7309, https://doi.org/10.1063/1.369353.
[34] Y. Liu, S. He, Development of low loss Mn–Zn ferrite working at frequency higher than 3MHz, J. Magn. Magn. Mater. 320 (23) (2008) 3318–3322, https://doi.org/10.1016/j.jmmm.2008.07.001.
[35] A. Furuya, et al., Magnetic field analysis for dimensional resonance in Mn–Zn ferrite toroidal core and comparison with permeability measurement, vol. PP, pp. 1–1, IEEE Trans. Magn. (2017), https://doi.org/10.1109/TMAG.2017.2713416.
[36] H. Kawano, et al., Systematic experimental and simulation studies of dimensional resonance in Mn-Zn Ferrite toroidal cores, 2018 IEEE Int. Magn. Conf. INTERMAG (2018) 1–5, https://doi.org/10.1109/INTMAG.2018.8508440.
[37] H.P. Rimal, G. Stornelli, A. Faba, E. Cardelli, Macromagnetic approach to the modeling in time domain of magnetic losses of ring cores of soft ferrites in power electronics, IEEE Trans. Power Electron. 38 (3) (2023) 3559–3568, https://doi.org/10.1109/TPEL.2022.3223184.